Retinalike Foveated Imaging through an Opaque Scattering Medium

Guangdong Ma, Shupeng Zhao⬤, Xiao Wang⬤, Zhihui Liang, Yufeng Qian, Jingjing Zhang,
Pei Zhang⬤, Hong Gao, Ruifeng Liu⬤,[*] and Fuli Li[†]

Ministry of Education Key Laboratory for Nonequilibrium Synthesis and Modulation of Condensed Matter,
Shaanxi Province Key Laboratory of Quantum Information and Quantum Optoelectronic Devices, School of
Physics, Xi'an Jiaotong University, Xi'an 710049, China

Imaging through an opaque scattering medium, such as biological tissue, is of broad interest for many applications from physics to life sciences. Measuring the transmission matrix (TM) of the scattering medium is a versatile tool for this purpose. Previously, researchers are used to improving the image resolution by measuring a gigantic TM with a long sampling time. However, the low resolution and low SNR of the reconstructed images are still two obstacles to the adoption of such a technique. The foveal centralis of the human eye produces sharper vision than that from the retina's peripheral region. Inspired by this feature, we report the implementation of foveated scattering imaging with a multiresolution TM whose space-variant resolution feature can be flexibly adjusted. The enhancement of linear resolution and SNR of the foveated scattering imaging system by factors of 4 and 8.3, respectively, is demonstrated experimentally. Our bioinspired imaging method heuristically introduces foveal vision into scattering imaging, and thus paves the way for both high resolution and high SNR imaging through scattering medium concurrently monitoring the entire field of view.

I. INTRODUCTION

High-resolution imaging through an opaque scattering medium is a fundamental problem for a variety of applications, ranging from microscopy [1], endoscopy [2], and astronomy [3]. Light encountering refractive-index inhomogeneities cause multiple scattering, so the information will be scrambled into disordered interference patterns named laser speckles [4]. Nonetheless, the process of multiple scattering in the time scale when the scattering medium keeps stable is deterministic, information conveyed inside such a medium is shuffled but conserved. Great research efforts [5] have resulted in the development of imaging through scattering medium in the last few decades, such as time gating and ballistic light imaging [6–9], optical wave-front-shaping techniques [10–14], speckle correlations and memory effects [15,16], transmission-matrix- (TM) based imaging [17–24], deep learning approaches [25–27].

The TM contains all the information, which relates the input to output channels of a scattering medium. The capability of TM to inverse the effect of scattering and efficiently focus light has been shown [28,29], further demonstrating its ability to reconstruct images through the scattering medium [17–24]. What is more, the information-rich and dimension-high nature of the TM enables manipulation of the light field in the scattering medium. Examples include the optimization of the energy transport inside the disordered medium [30–32], speckle engineering [33,34], and the creation of innovative forms from classical [35] to quantum information processing [36].

However, to fully sample an unknown scene to a particular resolution, the minimum input dimension of the TM should be equal to the total number of pixels of the reconstructed images. Limited by the speed of devices for wave-front modulation [37] and stable time of the scattering medium [38,39], the input dimension of TM is usually set about 10^3 in experiments [17,19–23]. In Ref. [18], the authors measured a gigantic TM (the input dimension about 20 000) to reconstruct a high-resolution (HR) image. In the TM-based imaging methods, doubling the linear resolution increases the required number of measurements (input dimension of TM) by a factor of 4, leading to a longer imaging time. This trade-off between resolution and imaging time sets the main obstacle for imaging through the scattering medium with the TM technique.

To address the above challenge, it makes sense to look for solutions presented in biological systems, on account of millions of years of evolution [40–43]. For example, the visual system of many animals characterizes a nonuni-

---

[*]ruifeng.liu@mail.xjtu.edu.cn
[†]flli@mail.xjtu.edu.cn

form structure, the center part of which represents more densely and acutely called the foveal [44]. Particularly, in the case of humans, the retinas present a unique high-resolution area in the center of the field of view (FOV) to accomplish complex visual tasks [45,46]. Behavioral experiments have shown that the distribution of receptive fields within the retina is fixed and the fovea can be redirected to other targets by ocular movements [46]. Even though foveal vision plays a key role in active target tracking [47], three-dimensional display [48], perception [49], and single-pixel imaging [50,51], it has not been explored when strong scattering medium exists in an imaging system.

Inspired by the specialized structure of the vertebrate eye, here, we come up with a mathematical model for foveated sampling and demonstrate a retinalike foveated scattering imaging with enhanced resolution and SNR. Instead of measuring TM with a uniform resolution, a reformatted TM with the spatially variant resolution is measured, as a result, we can obtain an image with double linear resolution in the foveal region first. Combined with the digital microscanning technique, the enhancement of linear resolution and SNR of the foveal scattering imaging system by factors of 4 and 8.3, respectively, is demonstrated experimentally. A dual foveated scattering imaging system is also implemented, which shows that the number and position of the region of interest (ROI) viewed in high resolution can be adjusted flexibly. Our proposal provides more degrees of freedom for customizing retinalike patterns and enables imaging through an opaque scattering medium with high resolution and high SNR in the ROI.

II. PRINCIPLE AND EXPERIMENTAL RESULTS

A. The principle of retinalike foveated sampling

Retinalike imaging theory and the system [52,53], of which the most remarkable property lies in the space-variant distribution of photoreceptor cells in the retina, has been studied for several decades. The schematic diagram of the retinalike structure is shown in Fig. 1. A unique HR area, called the foveal, locates in the center of the visual field (green part of Fig. 1), while coarse resolution areas are located in the peripheral region. This property may permit local resolution enhanced imaging through an opaque scattering medium representations and processing methodologies.

Figure 1(a) illustrates a rigorous log-polar sampling for retinalike imaging [53]. However, the sectors (*N*) for each ring are fixed and one cannot control the image resolution in different rings. We come up with a flexible sampling strategy by adjusting the number of sectors in the peripheral region as shown in Fig. 1(b). Our sampling scheme is
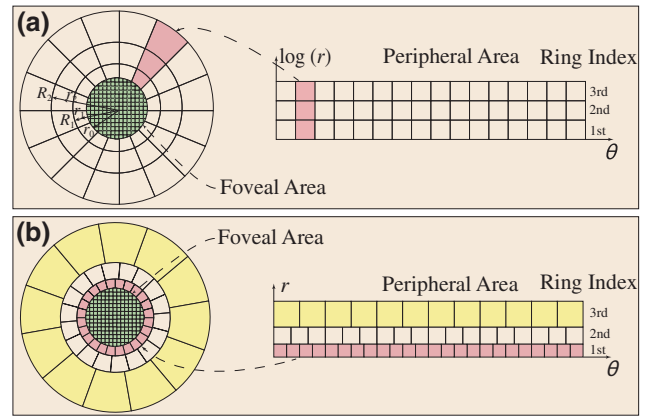

FIG. 1. Schematic of retinalike structure. (a) Log-polar sampling for retinalike imaging. (b) Flexible sampling for retinalike imaging.

modeled as

$$
\begin{aligned}
r_i &= \frac{r_{i-1} + R_{i-1}}{1 - \sin(\pi/N_i)} \\
R_i &= r_i \sin(\pi/N_i) \quad , \quad i \in \{1, 2, 3, \ldots\}; \\
R_0 &= 0
\end{aligned}
\tag{1}
$$

where N_i is an adjustable number corresponding to the sector number of *i*th ring. The center r_i and radius R_i of each ring are determined by the sector number N_i and the radius of the foveal region r_0 (green part of Fig. 1). This optimization results over the previous retinalike strategy [54,55], which scans the peripheral area with the fixed growing coefficient and sector [Fig. 1(a)]. On the other hand, the flexible sampling strategy proposed here permits a quasisquare sampling by a weak constrain in the second line of Eq. (1) and provides more degrees of freedom to customize patterns as well.

In previous work [17–22], the TMs were measured by a set of bases with uniform resolution. This measuring strategy results in reconstructed images with uniform resolution and SNR. Inspired by the above retinalike foveated sampling method, one may measure the TM with a set of multiresolution bases, and implement imaging through an opaque scattering medium with higher resolution and SNR in the ROI.

B. Retinalike foveated scattering imaging

The schematic of scattering imaging used in this work is depicted in Fig. 2. As shown in Figs. 2(a)–2(c), a SLM is placed on one side of a scattering medium (Scat) to encode the input light, and a CCD to record the speckle intensity pattern is placed on the other side of the medium. For the calibration of TM (see Appendix for details), a set of 32 × 32 Hadamard bases [Fig. 2(e)] are chosen, each of which is uniformly distributed on a mask with 32 × 32-cell grid
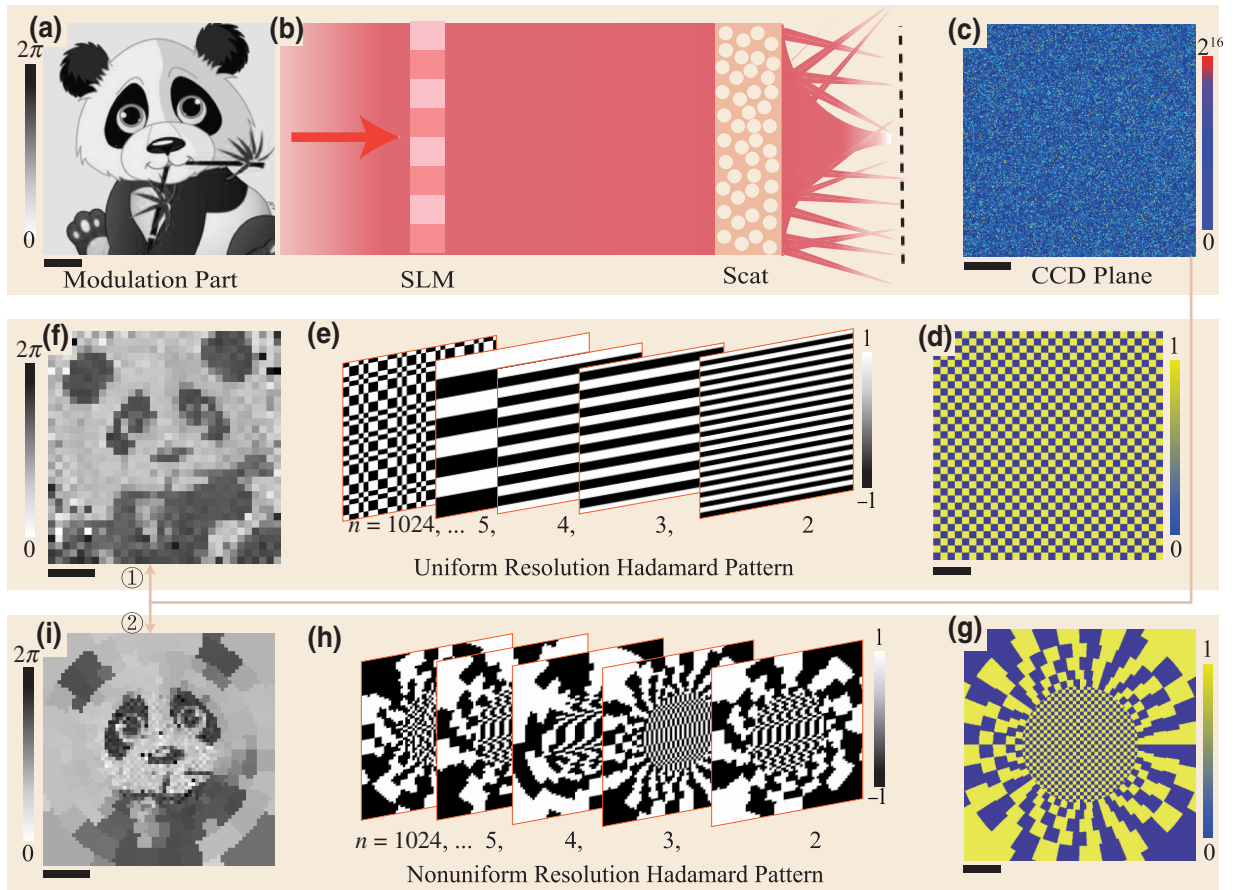
FIG. 2.   Schematic of scattering imaging with spatially uniform and variant resolution. (a) The original image. (b) A spatial light modulator (SLM) is placed on one side of the scattering medium (Scat) to encode the wave front of the incident light field, then the speckle intensity patterns are recorded by a CCD in (c). (d) 32×32-cell mask with uniform resolution. (e) Examples of 1024 Hadamard patterns formatted onto the two-dimensional (2D) uniform mask in (d). (f) Image of a panda reconstructed by Hadamard-basis TM with uniform resolution via ①. (g) The nonuniform resolution mask contains 1024 cells of spatially varying areas. (h) Examples of 1024 spatially variant Hadamard patterns reformatted onto the 2D nonuniform mask in (g). (i) Experimental result by the rearranged Hadamard-basis TM (via ②) and the linear resolution in the foveal region is twice that in (f). Both images of (f),(i) have the same FOV. Scale bar, 0.8 mm.

as shown in Fig. 2(d). The scattering medium can act as an imaging lens once the TM is obtained. The TM, denoted as **T**, relates the input field **X** to the output field **Y** by

$$\mathbf{Y} = \mathbf{TX}, \tag{2}$$

consequently, the knowledge of the transmitted intensity and the TM enables one to reconstruct the original image. In the experiments, we apply an alternating-iterative phase-retrieval algorithm to reconstruct the original image (see Appendix for details). Figure 2(f) shows one example of the experimentally retrieved image with a uniform resolution based on the Hadamard-basis transmission matrix (HTM) via ①. It provides barely any information about the panda's eyes and nose because of the limited number of measurements based on the feature of uniform resolution over the entire FOV.

Inspired by the multiresolution characteristic of foveal vision, higher resolution in the center, and lower resolution in the peripheral region (Fig. 1), a set of reformatted Hadamard-basis shown in Fig. 2(h) are used to measure the TM of the scattering medium. Then one can retrieve an image depicted in Fig. 2(i) with the nonuniform resolution based on the reformatted Hadamard-basis transmission matrix (RHTM) via ②. In this case, each modified basis is created by reformatting the corresponding Hadamard basis into a 2D mask with spatially variant cell size. Figure 2(g), generated by Eq. (1), shows an example mask used in experiments. The size of the cells is uniform in the central region and gradually increases in the peripheral region. Note that the mask in Fig. 2(g) contains 1024 independent cells, which is the same number of independent cells as the uniform resolution Hadamard basis in Fig. 2(d). However, the cell size in the central region of Fig. 2(g) is half of that in Fig. 2(d). Therefore, we expect a local resolution
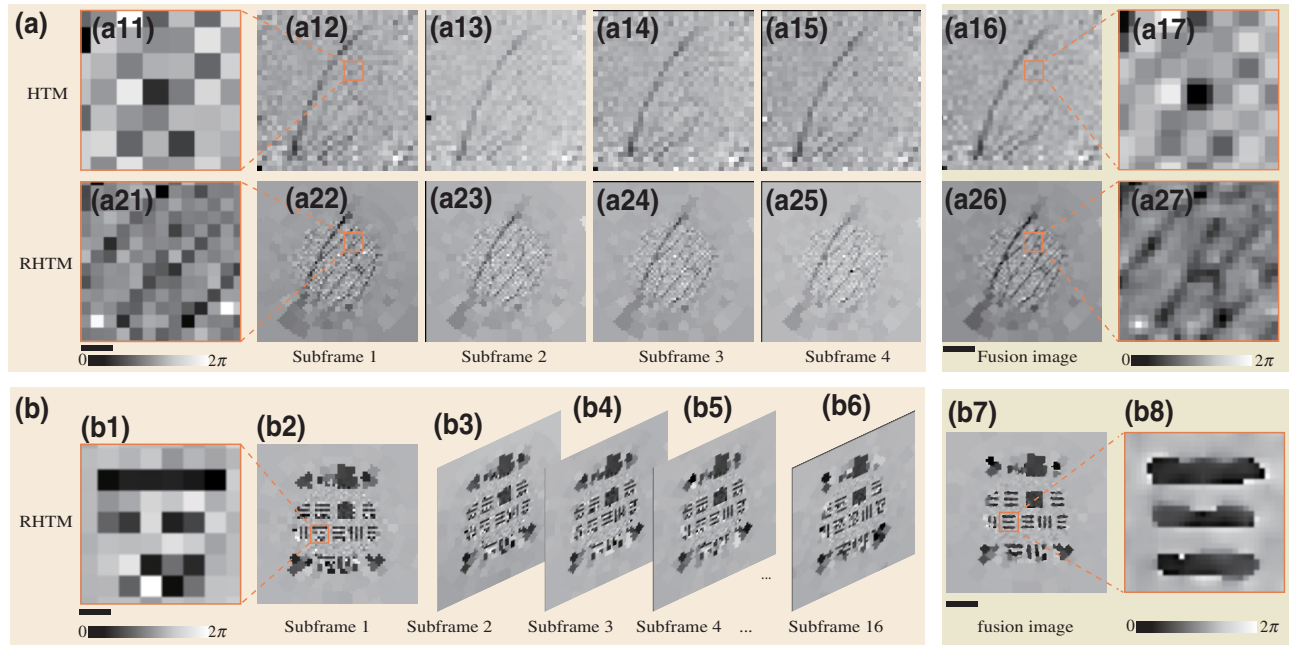
FIG. 3.   Experimental results of resolution-enhanced foveated scattering imaging with digital microscanning. (a) Reconstructed images of two times digital microscanning based on HTM, and RHTM. (a12)–(a15) and (a22)–(a25) are subframes of LR images. (a16),(a26) are fusion images, (a11),(a21) are partial enlarged view of (a12),(a22), (a17),(a27) are partial enlarged view of (a16),(a26). (b) Four times digital microscanning imaging results based on RHTM. (b2)–(b6) are subframes of LR images. (b7) is the fusion result, (b1),(b8) are partially enlarged views of (b2),(b7). Scale bar, 0.8 mm.

enhanced image by a factor of 2 with these reformatted Hadamard basis.

C. Resolution-enhanced foveated scattering imaging

HR image reconstruction is highly desirable for obtaining more structure details when seeing beneath the scattering medium (e.g., deep-tissue imaging). The main efforts to increase the spatial resolution of an image for a fixed FOV involve reducing the pixel size (increasing the number of pixels per cell area) in the process of manufacture and fully sampling the scene with a mass of patterns in experiments (e.g., measuring a larger TM [24]). However, measuring a larger TM gives rise to a longer imaging time, which demands a longer stable time of the scattering medium [56]. If N times the original linear resolution is expected, N^2 times the original imaging time is needed. This time-consuming process is not acceptable for deep-tissue imaging with TM, especially for biological tissues with a short decoherence time. Meanwhile, the decrease in pixel size may severely degrade the image SNR [57], and undo the former effort for spatial resolution enhancement. One promising approach for overcoming the above obstacles is to use the digital microscanning technique to obtain a HR image from multiple low-resolution (LR) images [58]. The underlying principle of digital microscanning is that each subframe samples complementary information of

the raw image, then one can combine these measurements to reconstruct a resolution-enhanced image.

Figure 3 illustrates how the digital microscanning method can be applied to foveated scattering imaging to improve the spatial resolution further. To achieve a double digital superresolution (DSR) image, the original image (insect's wing) is translated by half a cell's width in the x (or/and y) direction with respect to the other subframes (see Appendix for details). Figure 3(a) shows the DSR images by HTM (the first row) and RHTM (the second row). Figure 3(a12) is the reconstructed LR image without translation, and half a cell's width in the x (or/and y) direction exists among another three reconstructed LR images in Figs. 3(a13)–3(a15) (black area), respectively. After acquiring these four LR images, a simple fusion strategy, weighted averaging (see Appendix for more details), is applied to retrieve the HR image shown in Fig. 3(a16). The resolution of the fused image is twice that of the original LR images. Figures 3(a11) and 3(a17) are partially enlarged views of Figs. 3(a12) and 3(a16). Since the feature size of the textures in the wing approaches the size of sampling cells, the retrieved images with uniform resolution over the entire FOV based on HTM provides rarely useful information. Figures 3(a21)–3(a27) are counterparts of Figs. 3(a11)–3(a17), which are retrieved by RHTM. In the foveal region, the four subframes shown in Figs. 3(a22)–3(a25) are equal weighted, promoting a twice local resolution composite image in Fig. 3(a26). Due to the
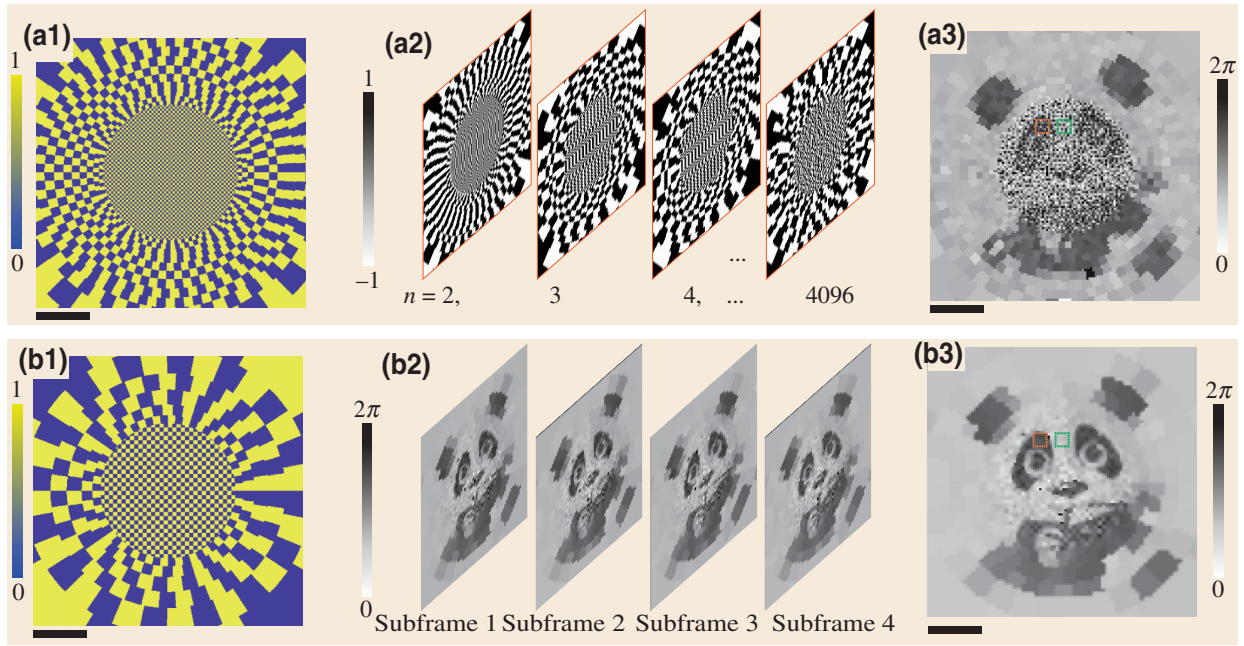
FIG. 4.   Experimental results of SNR-enhanced foveated scattering imaging with digital microscanning. (a1) A nonuniform resolution grid contains 4096 independent cells with the varying area. (a2) A set of spatially variant Hadamard patterns. (a3) Retrieved image by the large RHTM. (b1) A nonuniform resolution grid contains 1024 independent cells with the varying area. (b2) Four subframes of LR images. (b3) Fusion image by digital microscanning. Scale bar, 0.8 mm.

multiresolution feature of foveal vision, the detailed textures in the foveal region of the wing can be distinguished visually as shown in Fig. 3(a27).

Furthermore, a fourfold DSR is achieved by the scheme mentioned above. One needs to retrieve 16 subframes in this case, and there is a quarter-cell relative displacement in the x (or/and y) direction between subframes shown in Figs. 3(b2)–3(b6). Thus the linear resolution is increased fourfold in the foveal region of Fig. 3(b7) by combining the 16 LR subframes. The enlarged view in Fig. 3(b8) shows clear three lines, which cannot be distinguished in the enlarged view in Fig. 3(b1).

In the above foveated imaging process, a lower-dimensional TM with N columns is measured first. Then, a double DSR image can be obtained by the digital microscanning technique. The imaging time of this process scale with $N + 4$ where we omit the process of four-step phase shift for TM calibration. However, if one wants to get a double DSR image without the help of digital microscanning, a higher-dimensional TM with $4N$ columns is demanded and the imaging time for scattering imaging scale with $4N + 1$. So, the digital microscanning method is a good candidate for resolution-enhanced foveated scattering imaging without significantly increasing the imaging time.

D. SNR-enhanced foveated scattering imaging

Usually, the SNR of the reconstructed image decreases as its spatial resolution increases due to inevitable noise in experiment. There are two main sources of noise, illumination noise derived from fluctuations in light intensity during the measurement of TM and detector noise associated with the photodetector itself. The compromise between the image resolution and the SNR is one of the main drawbacks of scattering imaging. In this subsection, we show that it is possible to enhance both the resolution and SNR of the foveated scattering imaging at the same time.

The SNR of the reconstructed images with and without DSR under the same image resolution is studied in Fig. 4. The first row illustrates the process of image reconstruction by RHTM, and the input dimension of RHTM is 4096 in this case. To compare the SNR at the same image resolution, the second row shows the image reconstructed by RHTM as well, but with the digital microscanning technique. The input dimension of this RHTM is 1024. Both of these two RHTMs are encoded within the same size of FOV. Figures 4(a1) and 4(b1) show two spatially variant resolution cell grids, and they contain 4096 and 1024 independent cells with varying areas, respectively. A set of modified Hadamard patterns are shown in Fig. 4(a2). Figure 4(a3) shows the reconstructed image. Fusing four LR images in Fig. 4(b2), an HR image is obtained once again as shown in Fig. 4(b3). Therefore, the linear resolution of the foveal region in Fig. 4(b3) is equal to that in Fig. 4(a3), which is reconstructed by RHTM with 4096 input bases. For each reconstructed image, the SNR is calculated by $\mathrm{SNR} = 2(\langle I_s \rangle - \langle I_b \rangle)/(\sigma_s + \sigma_b)$, where $\langle I_s \rangle$ and $\langle I_b \rangle$ are the average intensity of the signal and background
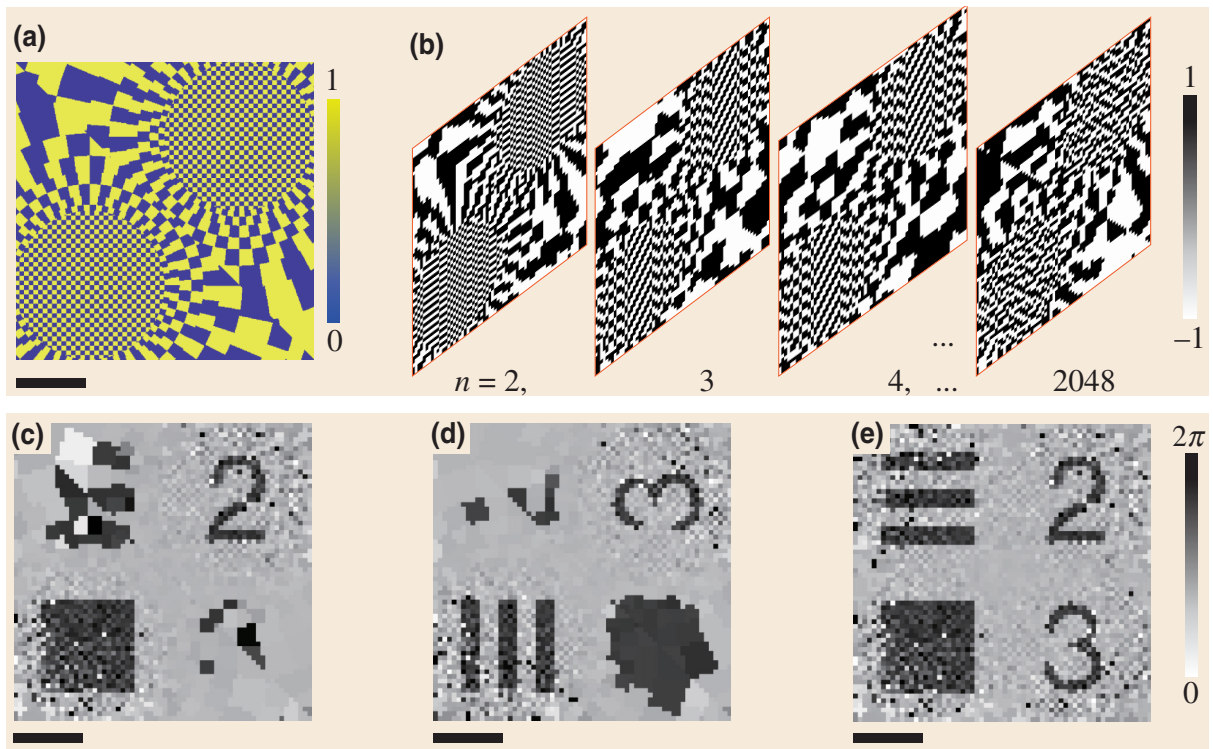
FIG. 5. Experimental results of dual foveated scattering imaging. (a) A nonuniform resolution grid contains 2048 independent cells with varying areas and a set of spatially variant Hadamard patterns (b). (c) The image is reconstructed by the dual foveal RHTM. (d) The retrieved image by rotating the image 90° clockwise. (e) The image after (d) is rotated 90° counterclockwise and fused with (c). Scale bar, 0.8 mm.

area, respectively, σ_s and σ_b are the standard deviation of the signal and background area, respectively, [green and orange square in Figs. 4(a3) and 4(b3)].

The SNRs are 3.60 and 29.02 for Figs. 4(a3) and 4(b3), respectively, yielding an increase of 8.3 times for the digital microscanning method. The experimental results show that the SNR of the image reconstructed by digital microscanning is remarkably higher than that of the image reconstructed by the larger TM. The improvement of SNR is attributed to the stochastic nature of noise. Meanwhile, the linear resolution in the foveal region of Fig. 4(b3) is 4 times that of Fig. 2(f). Therefore, incorporated with the digital microscanning technique, the retinalike foveated scattering imaging system does offer an enhancement of both spatial resolution and SNR of the reconstructed images.

E. Dual foveated scattering imaging

In addition to single foveal vision, a dual foveated scattering imaging system is implemented where we keep the same size of FOV as the above experiments. Figure 5(a) shows a nonuniform resolution grid containing 2048 independent cells, and two foveal regions occupy the regular square grids. Figure 5(b) shows a set of reformatted Hadamard bases, and each of these patterns contains two

foveal regions along the diagonal direction. Once these reformatted Hadamard bases are loaded sequentially on the SLM, the full RHTM can be obtained. Then, the reconstructed image as depicted in Fig. 5(c) can be obtained by the RHTM and alternating-iterative phase retrieval algorithm. Since only two foveal areas provide HR image information about the original target, the image information in the antidiagonal direction can not be retrieved precisely. By rotating the original image 90° clockwise, one can obtain a complementary diagonal image as shown in Fig. 5(d). Then, Fig. 5(d) is rotated 90° counterclockwise and fuses it with Fig. 5(c), one can obtain all the information about the target as shown in Fig. 5(e).

III. CONCLUSION

In conclusion, we demonstrate that the local resolution and SNR of scattering imaging with the same size of FOV can be enhanced simultaneously by mimicking the foveal vision of the vertebrate eye. To get a more flexible retinalike sampling, we come up with a mathematical model and elaborately design a flexible multiresolution sampling strategy for the foveated scattering imaging system. As a result, the resolution of the retrieved image is doubled in the foveal region compared with the traditional method. Furthermore, we simultaneously enhance linear resolution

and SNR of the foveated scattering imaging system by factors of 4 and 8.3 in experiments with digital microscanning. The flexible retinalike sampling strategy proposed here provides more degrees of freedom to customizing retinalike patterns. The bioinspired imaging method deployed here is universal to any form of computing imaging that relies on sequential correlation measurements. As such, it would be appealing to introduce retinalike foveated imaging to biomedical applications, microendoscopy, photoacoustic imaging, or fluorescence imaging, where the disturbances of opaque scattering medium cannot be neglected. A combination of biomimetic and scattering media, as well as efficient computation, might lead to alternative forms of imaging prototypes, and this is an area that remains explored.

APPENDIX

1. Experimental setup and TM calibration

The experimental setup is depicted in Fig. 6(a). A collimated He-Ne laser (633 nm, LASOS 7470 A4) illuminates the phase-only SLM (Holoeye PLUTO-VIS-016) with a resolution of 1920×1080 pixels. For the calibration of TM, a total of 628×628 pixels on the SLM are used to modulate the input light field, of which 512×512 pixels [purple segment in Fig. 6(b)] in the central region are the signal part. The Hadamard patterns and original images are encoded in this signal region. The other is a reference part [cyan segment in Fig. 6(b)] loaded with a static pattern surrounding the central area. After being modulated, the light passes through a 4f telescope system, and an aperture filter is placed at the Fourier plane of L1 to select the +1-order diffracted light only. Then, the light is focused onto the front surface of the scattering medium, ground glass (120 Grit, Edmund), by an objective lens (Olympus, RMS $10 \times /0.25$). Transmitted light is collected by another objective lens (Olympus, RMS $10 \times /0.25$) placed behind the scattering medium. The intensity pattern depicted in Fig. 6(c) is recorded by a CCD (Lumenera INFINITY3S-1UR). Because the information of the original image is highly redundant in the speckle pattern [26], only the target part of the speckle image is cropped as illustrated in Fig. 6(c) (blue box). To suppress correlation among neighboring pixels further, we downsample every speckle pattern into 256×256 pixels, which is in terms of the average size of the speckle grains.
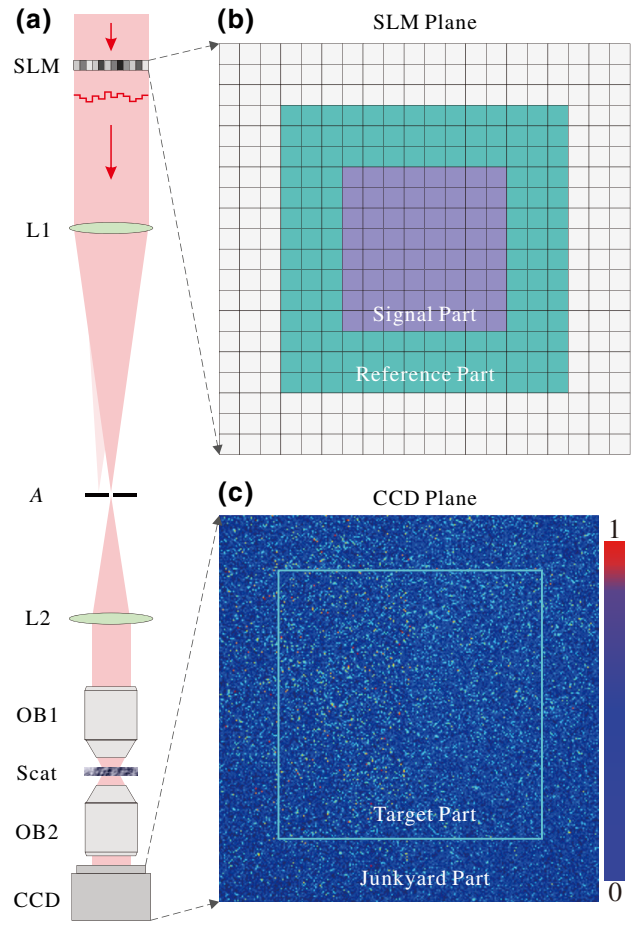

FIG. 6. (a) Experimental setup. A He-Ne laser (632.8 nm) used as light source, SLM, spatial light modulator; L1, L2, lens; A, aperture; OB1, OB2, object lens; Scat, ground glass; CCD, charge-coupled device. (b) SLM plane for TM calibration and imaging, the center purple part of SLM is the signal part. In the peripheral part denoted with a cyan color, the beam is projected as a static reference field. (c) Experimentally measured speckle pattern and only the center area is cropped for data processing.

As a result, each remaining pixel corresponds to one output mode [59]. Each of these measurements returns one column of the TM. In the experiments, the four-step phase-shift method is used to measure the complex optical field of the speckles. Once the input patterns cover the whole bases for the input light field, the full TM can be obtained [28].

2. Phase-retrieval algorithm

The underlying principle of the linear scattering system can be taken as a deterministic process in mathematics $\mathbf{Y} = \mathbf{TX}$, where $\mathbf{Y} = [y_1, y_2, \ldots, y_M]^{\mathrm{T}} \in \mathbb{C}^{M \times 1}$, and $\mathbf{X} = [x_1, x_2, \ldots, x_N]^{\mathrm{T}} \in \mathbb{C}^{N \times 1}$ are the output and input complex fields, respectively. M and N are the numbers of pixels on the CCD plane and SLM plane. $\mathbf{T} \in \mathbb{C}^{M \times N}$ is a forward propagation operator, i.e., TM in this paper, connecting

Algorithm 1 Alternating-iterative phase retrieval algorithm.

Input:
    The amplitude of speckle pattern, $|\mathbf{Y}|$;
    The TM of scattering system, $\mathbf{T}$;
    The maximum number of iterations, maxiter;
Output:
    The object to be reconstructed, $\mathbf{X}$;
1: $\mathbf{X_0} \leftarrow \mathbf{T^{-1}}|\mathbf{Y}| \cdot \exp(\phi)$ {Initialize $\mathbf{X}$ with a random matrix ϕ}
2: **for** $\mathbf{i} = 1$ to maxiter **do**
3:    $\mathbf{Y_i} \leftarrow |\mathbf{Y}|^2 \cdot \exp(i \cdot \arg(\mathbf{TX_{i-1}}))$ {Impose constraints $|\mathbf{Y}|^2$}
4:    $\mathbf{X_i} \leftarrow \mathbf{TY_i}$
5:    $\mathbf{Y_i} \leftarrow |\mathbf{Y}| \cdot \exp(i \cdot \arg(\mathbf{TX_i}))$ {Impose constraints $|\mathbf{Y}|$}
6:    $\mathbf{X_i} \leftarrow \mathbf{TY_i}$
7: **end for**
8: **return** $\mathbf{X}$;

FIG. 7. Flow chart of the alternating-iterative phase-retrieval algorithm.

the input field loaded upon the SLM plane to the recorded intensity pattern $|\mathbf{Y}|^2$ at the CCD plane. There are various algorithms to estimate $\mathbf{X}$ from $|\mathbf{Y}|^2$ and $\mathbf{T}$, such as the Gerchberg-Saxton algorithm [60], Fienup algorithm [61], and Wirtinger Flow algorithm [62]. Here, we implement an alternating-iterative phase-retrieval algorithm to reconstruct the scattering images. The flow chart of the algorithm is summarized in Fig. 7, where "·" stands for elementwise multiplication, and "arg()" computes the principal value of the argument of a complex number. In the beginning, the object to be recovered is randomly initialized as $\mathbf{X_0}$. In each iteration, two steps of constraints are imposed to speed up the convergence. The first step uses $|\mathbf{Y}|^2$ to impose constraints on the detector plane. In the second step, the power of $|\mathbf{Y}|$ decreases to 1 by taking the square root of the speckle captured by the CCD.

3. Digital microscanning

The schematic of digital microscanning is shown in Fig. 8. 2×2 pixels are combined as a superpixel in each subframe, so each pixel in one superpixel has the same intensity value, providing no information about how the intensity values may be distributed between the adjacent pixels within the superpixel. Fortunately, subsuperpixel's width shift can be implemented in the x (or/and y) direction for each subframe. The final HR image can be obtained by registering the LR images over a HR grid and then averaging them.

In this paper, a weighted average strategy is adopted to stitch multiple subframes. Therefore, the value of the center pixel in the right part of Fig. 8 on the HR grid is computed as $I_{\text{cen}} = (I_a + I_b + I_c + I_d)/4$, where I is the intensity value at different regions and the denominator 4 denotes the number of pixels in the overlapping region. The fact that combining 2×2 pixels as a superpixel is used for pattern shift is for convenience. Beyond the weighted averaging fusion strategy described here, more
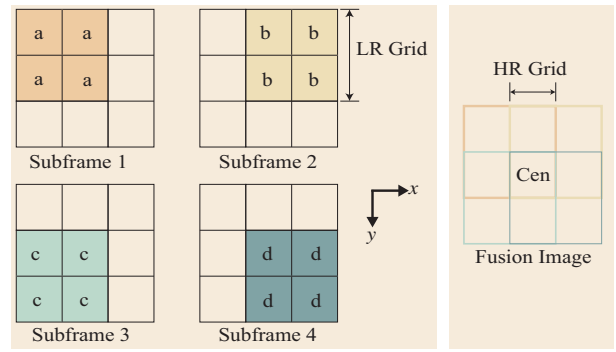

FIG. 8. Schematic of the digital microscanning method. The left part shows four LR subframes, and there is a relative displacement of the half cell (2×2 pixels are combined as a superpixel) in the x (or/and y) direction between each of these LR images, the right part shows the fusion HR image, and the length of the HR grid is half that of the LR grid.

sophisticated fusion algorithms are also compatible for this purpose [63].

In the experiments, 512×512 pixels on the SLM are selected as the signal region to encode the input bases and original images (see Appendix for details). The area of this 512×512-pixel region is 4.096×4.096 mm^2, and all the original images in the following experiments keep the same size as this signal region. For the HTM calibration, 16×16 pixels on the SLM plane are combined as a cell, which results in a 32×32-cell grid. While for the calibration of RHTM, the 512×512-pixel region is divided into 1024 spatially variant cells based on the mask of Fig. 2(g). In the central region with a uniform resolution, each cell is constructed by combining 8×8 pixels on the SLM, and any spatial frequency components that exceed the spatial frequency of the 2D grid are lost in this process. Figures 2(f) and 2(i) show the reconstructed images with uniform and nonuniform resolution based on HTM and RHTM, respectively. Although the same measurement resources, that is the same total number of independent cells (1024) and the dimension of the TM, are used for both of the retrieved images with the same FOV, the linear resolution in the foveal region, where the cells occupy a regular square grid, of Fig. 2(i) is twice that of Fig. 2(f). The detail of the panda's eyes and nose of Fig. 2(i) in the foveal region are therefore more distinct than that in Fig. 2(f) at the expense of lower peripheral resolution.

[1] V. Ntziachristos, Going deeper than microscopy: The optical imaging frontier in biology, Nat. Methods **7**, 603 (2010).

[2] S. Turtaev, I. T. Leite, T. Altwegg-Boussac, J. M. Pakan, N. L. Rochefort, and T. Čižmár, High-fidelity multimode fibre-based endoscopy for deep brain in vivo imaging, Light: Sci. Appl. **7**, 1 (2018).

[3] H. W. Babcock, Adaptive optics revisited, Science **249**, 253 (1990).

[4] J. W. Goodman, *Speckle Phenomena in Optics: Theory and Applications* (SPIE Press, Bellingham, 2020), https://spie.org/Publications/Book/2548482?SSO=1.

[5] S. Gigan, O. Katz, H. B. de Aguiar, E. R. Andresen, A. Aubry, J. Bertolotti, E. Bossy, D. Bouchet, J. Brake, S. Brasselet *et al.*, Roadmap on wavefront shaping and deep imaging in complex media, J. Phys.: Photonics **4**, 042501 (2022).

[6] L. Wang, P. Ho, C. Liu, G. Zhang, and R. Alfano, Ballistic 2-d imaging through scattering walls using an ultrafast optical Kerr gate, Science **253**, 769 (1991).

[7] A. Velten, T. Willwacher, O. Gupta, A. Veeraraghavan, M. G. Bawendi, and R. Raskar, Recovering three-dimensional shape around a corner using ultrafast time-of-flight imaging, Nat. Commun. **3**, 1 (2012).

[8] D. B. Lindell and G. Wetzstein, Three-dimensional imaging through scattering media based on confocal diffuse tomography, Nat. Commun. **11**, 1 (2020).

[9] P. Pai, J. Bosch, M. Kühmayer, S. Rotter, and A. P. Mosk, Scattering invariant modes of light in complex media, Nat. Photonics **15**, 431 (2021).

[10] O. Katz, E. Small, and Y. Silberberg, Looking around corners and through thin turbid layers in real time with scattered incoherent light, Nat. Photonics **6**, 549 (2012).

[11] A. P. Mosk, A. Lagendijk, G. Lerosey, and M. Fink, Controlling waves in space and time for imaging and focusing in complex media, Nat. Photonics **6**, 283 (2012).

[12] I. N. Papadopoulos, S. Farahi, C. Moser, and D. Psaltis, High-resolution, lensless endoscope based on digital scanning through a multimode optical fiber, Biomed. Opt. Express **4**, 260 (2013).

[13] K. Si, R. Fiolka, and M. Cui, Fluorescence imaging beyond the ballistic regime by ultrasound-pulse-guided digital phase conjugation, Nat. Photonics **6**, 657 (2012).

[14] X. Yang, C.-L. Hsieh, Y. Pu, and D. Psaltis, Three-dimensional scanning microscopy through thin turbid media, Opt. Express **20**, 2500 (2012).

[15] J. Bertolotti, E. G. Van Putten, C. Blum, A. Lagendijk, W. L. Vos, and A. P. Mosk, Non-invasive imaging through opaque scattering layers, Nature **491**, 232 (2012).

[16] O. Katz, P. Heidmann, M. Fink, and S. Gigan, Non-invasive single-shot imaging through scattering layers and around corners via speckle correlations, Nat. Photonics **8**, 784 (2014).

[17] S. Popoff, G. Lerosey, M. Fink, A. C. Boccara, and S. Gigan, Image transmission through an opaque material, Nat. Commun. **1**, 1 (2010).

[18] Y. Choi, T. D. Yang, C. Fang-Yen, P. Kang, K. J. Lee, R. R. Dasari, M. S. Feld, and W. Choi, Overcoming the Diffraction Limit using Multiple Light Scattering in a Highly Disordered Medium, Phys. Rev. Lett. **107**, 023902 (2011).

[19] X. Tao, D. Bodington, M. Reinig, and J. Kubby, High-speed scanning interferometric focusing by fast measurement of binary transmission matrix for channel demixing, Opt. Express **23**, 14168 (2015).

[20] K. Lee and Y. Park, Exploiting the speckle-correlation scattering matrix for a compact reference-free holographic image sensor, Nat. Commun. **7**, 1 (2016).

[21] Y. Baek, K. Lee, and Y. Park, High-Resolution Holographic Microscopy Exploiting Speckle-Correlation Scattering Matrix, Phys. Rev. Appl. **10**, 024053 (2018).

[22] A. Boniface, J. Dong, and S. Gigan, Non-invasive focusing and imaging in scattering media with a fluorescence-based transmission matrix, Nat. Commun. **11**, 1 (2020).

[23] S.-J. Tu, X. Zhao, Q.-Y. Yue, Y.-J. Cai, C.-S. Guo, and Q. Zhao, Shaping the illumination beams for STED imaging through highly scattering media, Appl. Phys. Lett. **119**, 211105 (2021).

[24] H. Yu, T. R. Hillman, W. Choi, J. O. Lee, M. S. Feld, R. R. Dasari, and Y. Park, Measuring Large Optical Transmission Matrices of Disordered Media, Phys. Rev. Lett. **111**, 153902 (2013).

[25] N. Borhani, E. Kakkava, C. Moser, and D. Psaltis, Learning to see through multimode fibers, Optica **5**, 960 (2018).

[26] M. Lyu, H. Wang, G. Li, S. Zheng, and G. Situ, Learning-based lensless imaging through optically thick scattering media, Adv. Photonics **1**, 036002 (2019).

[27] Y. Li, S. Cheng, Y. Xue, and L. Tian, Displacement-agnostic coherent imaging through scatter with an interpretable deep neural network, Opt. Express **29**, 2244 (2021).

[28] S. M. Popoff, G. Lerosey, R. Carminati, M. Fink, A. C. Boccara, and S. Gigan, Measuring the Transmission Matrix in Optics: An Approach to the Study and Control of Light Propagation in Disordered Media, Phys. Rev. Lett. **104**, 100601 (2010).

[29] J. Xu, H. Ruan, Y. Liu, H. Zhou, and C. Yang, Focusing light through scattering media by transmission matrix inversion, Opt. Express **25**, 27234 (2017).

[30] M. Kim, Y. Choi, C. Yoon, W. Choi, J. Kim, Q.-H. Park, and W. Choi, Maximal energy transport through disordered media with the implementation of transmission eigenchannels, Nat. Photonics **6**, 581 (2012).

[31] P. Hong, O. S. Ojambati, A. Lagendijk, A. P. Mosk, and W. L. Vos, Three-dimensional spatially resolved optical energy density enhanced by wavefront shaping, Optica **5**, 844 (2018).

[32] H. Yılmaz, C. W. Hsu, A. Yamilov, and H. Cao, Transverse localization of transmission eigenchannels, Nat. Photonics **13**, 352 (2019).

[33] A. Boniface, M. Mounaix, B. Blochet, R. Piestun, and S. Gigan, Transmission-matrix-based point-spread-function engineering through a complex medium, Optica **4**, 54 (2017).

[34] L. Devaud, B. Rauer, J. Melchard, M. Kühmayer, S. Rotter, and S. Gigan, Speckle Engineering through Singular Value Decomposition of the Transmission Matrix, Phys. Rev. Lett. **127**, 093903 (2021).

[35] M. W. Matthès, P. del Hougne, J. de Rosny, G. Lerosey, and S. M. Popoff, Optical complex media as universal reconfigurable linear operators, Optica **6**, 465 (2019).

[36] S. Leedumrongwatthanakun, L. Innocenti, H. Defienne, T. Juffmann, A. Ferraro, M. Paternostro, and S. Gigan, Programmable linear quantum networks with a multimode fibre, Nat. Photonics **14**, 139 (2020).

[37] D. B. Conkey, A. M. Caravaca-Aguirre, and R. Piestun, High-speed scattering medium characterization with

application to focusing light through turbid media, Opt. Express **20,** 1733 (2012).

[38] M. M. Qureshi, J. Brake, H.-J. Jeon, H. Ruan, Y. Liu, A. M. Safi, T. J. Eom, C. Yang, and E. Chung, In vivo study of optical speckle decorrelation time across depths in the mouse brain, Biomed. Opt. Express **8,** 4855 (2017).

[39] Y. Liu, P. Lai, C. Ma, X. Xu, A. A. Grabar, and L. V. Wang, Optical focusing deep inside dynamic scattering media with near-infrared time-reversed ultrasonically encoded (true) light, Nat. Commun. **6,** 1 (2015).

[40] T. H. Goldsmith, Optimization, constraint, and history in the evolution of eyes, Q. Rev. Biol. **65,** 281 (1990).

[41] T. D. Lamb, S. P. Collin, and E. N. Pugh, Evolution of the vertebrate eye: Opsins, photoreceptors, retina and eye cup, Nat. Rev. Neurosci. **8,** 960 (2007).

[42] J. K. Bowmaker, Evolution of vertebrate visual pigments, Vision Res. **48,** 2022 (2008).

[43] M. S. Banks, W. W. Sprague, J. Schmoll, J. A. Parnell, and G. D. Love, Why do animal eyes have pupils of different shapes?, Sci. Adv. **1,** e1500391 (2015).

[44] M. F. Land and D.-E. Nilsson, *Animal Eyes* (Oxford University Press, Oxford, 2012).

[45] J. Hirsch and C. A. Curcio, The spatial resolution capacity of human foveal retina, Vision Res. **29,** 1095 (1989).

[46] J. Intoy, N. Mostofi, and M. Rucci, Fast and nonuniform dynamics of perisaccadic vision in the central fovea, Proc. Natl. Acad. Sci. **118,** e2101259118 (2021).

[47] S. Kamkar, F. Ghezloo, H. A. Moghaddam, A. Borji, and R. Lashgari, Multiple-target tracking in human and machine vision, PLoS Comput. Biol. **16,** e1007698 (2020).

[48] J. Hua, E. Hua, F. Zhou, J. Shi, C. Wang, H. Duan, Y. Hu, W. Qiao, and L. Chen, Foveated glasses-free 3d display with ultrawide field of view via a large-scale 2d-metagrating complex, Light: Sci. Appl. **10,** 1 (2021).

[49] S. Thiele, K. Arzenbacher, T. Gissibl, H. Giessen, and A. M. Herkommer, 3d-printed eagle eye: Compound microlens system for foveated imaging, Sci. Adv. **3,** e1602655 (2017).

[50] D. B. Phillips, M.-J. Sun, J. M. Taylor, M. P. Edgar, S. M. Barnett, G. M. Gibson, and M. J. Padgett, Adaptive foveated single-pixel imaging with dynamic supersampling, Sci. Adv. **3,** e1601782 (2017).

[51] X. Zhai, Z. dong Cheng, Y. di Hu, Y. Chen, Z. yu Liang, and Y. Wei, Foveated ghost imaging based on deep learning, Opt. Commun. **448,** 69 (2019).

[52] G. Sandini and G. Metta, Retina-like sensors: motivations, technology and applications, in Sensors and sensing in biology and engineering (Springer, Vienna, 2003), p. 251.

[53] V. J. Traver and A. Bernardino, A review of log-polar imaging for visual perception in robotics, Rob. Auton. Syst. **58,** 378 (2010).

[54] S. Li, J. Cao, Y. Cheng, L. Meng, W. Xia, Q. Hao, and Y. Fang, Spatially adaptive retina-like sampling method for imaging lidar, IEEE Photonics J. **11,** 1 (2019).

[55] Q. Hao, Y. Tao, J. Cao, M. Tang, Y. Cheng, D. Zhou, Y. Ning, C. Bao, and H. Cui, Retina-like imaging and its applications: A brief review, Appl. Sci. **11,** 7058 (2021).

[56] B. Blochet, K. Joaquina, L. Blum, L. Bourdieu, and S. Gigan, Enhanced stability of the focus obtained by wavefront optimization in dynamical scattering media, Optica **6,** 1554 (2019).

[57] R. N. Bryan, *Introduction to the Science of Medical Imaging* (Cambridge University Press, Cambridge, 2009).

[58] S. C. Park, M. K. Park, and M. G. Kang, Super-resolution image reconstruction: A technical overview, IEEE Signal Process. Mag. **20,** 21 (2003).

[59] C. W. Hsu, S. F. Liew, A. Goetschy, H. Cao, and A. Douglas Stone, Correlation-enhanced control of wave focusing in disordered media, Nat. Phys. **13,** 497 (2017).

[60] R. W. Gerchberg, A practical algorithm for the determination of phase from image and diffraction plane pictures, Optik **35,** 237 (1972).

[61] J. R. Fienup, Phase retrieval algorithms: A comparison, Appl. Opt. **21,** 2758 (1982).

[62] E. J. Candes, X. Li, and M. Soltanolkotabi, Phase retrieval via Wirtinger flow: Theory and algorithms, IEEE Trans. Inf. Theory **61,** 1985 (2015).

[63] K. Nasrollahi and T. B. Moeslund, Super-resolution: A comprehensive survey, Mach. Vis. Appl. **25,** 1423 (2014).